Plasma excitations in charged sodium clusters

J. Borggreen, P. Chowdhury,* N. Kebaïli,† L. Lundsberg-Nielsen,‡ K. Lützenkirchen,§ M. B. Nielsen, J. Pedersen, and H. D. Rasmussen

The Niels Bohr Institute, University of Copenhagen, DK-4000 Roskilde, Denmark

(Received 8 March 1993; revised manuscript received 13 September 1993)

Photoabsorption cross sections for free, singly charged sodium clusters (14–48 atoms) have been measured by recording the light-induced evaporation. The measurements cover the region from 366 nm (3.4 eV) to 605 nm (2.0 eV) in 15 steps with a spectral resolution of $\simeq 10$ nm. The evaporation residues are separated in an electrostatic field and detected by a position-sensitive microchannel plate. The spectra are dominated by surface-plasma oscillations of the valence electrons with a cross section that exhausts $\approx 70-100\,\%$ of the dipole sum rule. Over the mass range considered, the mean energies of the resonances are constant ($\simeq 2.64$ eV), and redshifted compared to the corresponding experimental bulk-plasmon energy but slightly blueshifted compared to the resonance energy of neutral clusters. A double structure of the resonance peak is observed for nonmagic clusters. It is discussed and interpreted in terms of spheroidal deformations.

I. INTRODUCTION

A fascinating aspect of a metal cluster, considered as a bound quantum state, is the interplay of single-particle and collective motion in the system. On one hand, the electronic shell structure leading to magic numbers of extra stability in the mass abundances can be understood in terms of the bunching of the quantum states of independent electrons in an effective potential, which includes contributions from both the ionic core and the electron-electron interactions.[1] This is analogous to the shell model for atomic nuclei, where the individual nucleons move in an effective mean field from all the remaining nucleons. On the other hand, photoabsorption studies have revealed collective excitations of metal clusters in the form of plasmon resonances.[2] This is interpreted as a dipole oscillation of the valence electron cloud with respect to the positive core, in analogy with the giant dipole resonance in nuclei, where the neutrons and protons oscillate collectively out of phase. In metallic clusters, the restoring force is the long-range Coulomb attraction between the constituents of opposite charge, whereas in atomic nuclei, it is the short-range attractive nuclear force between neutrons and protons.

A systematic investigation of the plasmon resonance as a function of cluster size will probe the static and dynamic properties of clusters as they evolve towards the bulk. The surface plasmon in a small spherical system is closely related to the bulk-plasma excitation of metals. As in the bulk, its frequency depends mainly on the density of the valence electrons and is therefore size independent to first order, with a frequency that is $1/\sqrt{3}$ of the bulk-plasma frequency. The measured resonance frequencies for small metallic clusters are, however, shifted to even lower values (see Refs. 3, 4, and references therein). This is likely to be due to the electron spill-out beyond the core of positive ions, thus decreasing the effective electron density and, in turn, the frequency of the surface plasmon.

The spectral profile of the resonance contains information on the shape of the clusters. Clusters with a closed shell of valence electrons are expected to be spherical, while clusters in between the magic numbers are likely to attain a deformed shape.[5] This is analogous to the Jahn-Teller effect in crystals or to deformations of open-shell atomic nuclei. While a spherical cluster has a single resonance frequency, a deformed cluster with axes of different lengths exhibits different resonance frequencies for electronic motion along these axes. This multiple structure of the resonance peak has been observed in a number of cases and attributed to axially deformed cluster shapes.[3,6–8]

The width of the individual resonance peaks provides insight into the interplay of the single-particle and the collective degrees of freedom in the cluster. Part of the width will be due to thermal broadening, but theoretical calculations involving random-phase and time-dependent local-density approximations (see Ref. 9 and references therein) also predict a temperature-independent broadening due to Landau damping, a fragmentation of collective strength onto near-lying excitations of a one-electron one-hole nature.

The present work—part of which was published previously[10]—systematically maps the photoabsorption spectrum of singly charged sodium clusters with 14 to 48 atoms, where the full energy region of the plasmon resonance is spanned in relatively fine steps. From the measurements the mean energies of the plasmon resonances are extracted, as well as the cross sections, both absolute and as a fraction of the dipole sum rule We find a constant resonance energy over the size range considered and with cross sections that exhaust the dipole sum rule for valence electrons by $\approx 70-100\,\%$. The spectral shapes are furthermore interpreted in terms of spheroidal distortions of the clusters. Because of the systematic variation of deformations over nearly two main shells this interpretation finds additional support in the present investigation.

The experimental arrangement is described in Sec. II, and the measurements and data analysis in Sec. III. The results are presented and discussed in Secs. IV and V.

II. EXPERIMENT

The photoabsorption cross section of a cluster at a given photon energy is determined by detection of the daughter clusters formed by evaporation of one or more atoms from the parent cluster. The essential components of the experimental arrangement developed for this purpose are sketched in Fig. 1 of Ref. 10.

Neutral clusters are formed by supersonic expansion of sodium vapor and argon gas through a nozzle of 70-μm diam and 100-μm length. The sodium vapor (at a partial pressure of about 100–200 mbar) is produced by heating sodium metal to temperatures of 700–750 °C, with the argon pressure adjusted at 4–5 bar.

After passing through two skimmers, with pumping in between, the sodium clusters enter a high-vacuum region ($\simeq 2\times 10^{-7}$ mbar). They travel at a speed of ≈ 1000 m/s for approximately 1 m before entering a drift tube of 10-cm length, held at a positive potential of 2 kV. The clusters are ionized by light which crosses the drift tube perpendicularly through holes of 1-cm diam. The light is obtained from a 1000-W high-pressure xenon arc lamp and is filtered (filter type UG 11) to a broadband spectrum of 3.6 ± 0.5 eV; the ionization threshold for the relevant cluster sizes lie between 3.4 and 3.7 eV.

On leaving the drift tube, the clusters are accelerated to an energy of 2 keV by an array of 36 electrodes whose respective potentials decrease from +2 kV to zero. The individual electrode potentials can be varied in order to optimize the focusing of the cluster beam.

Cluster ions of different masses are subsequently separated by a velocity filter of 20-cm length, consisting of crossed magnetic and electric fields. The magnetic field is created by permanent magnets. A field strength of 0.25 T is used to select clusters with less than 30 atoms, while a 0.83-T field is used for the larger ones. The electric field is adjusted in order to select a specific velocity and, in turn, guide a specific mass through a vertical collimator of 2 mm placed 1 m further downstream. The resolution of the 0.25-T velocity filter is illustrated in Fig. 1.

The mass-selected cluster beam is then crossed by monochromatic light, obtained by filtering the continuous spectrum from a second xenon arc lamp (1000 W) with interference filters. A wavelength range from 366 to 605 nm is covered with 15 filters each having a transmission with full width at half maximum of about 10 nm. The filters are mounted on two wheels, rotated by stepping motors in such a way that the filters intercept the light beam for 5 s each. In addition, a nontransmitting metal plate is mounted on one of the wheels in order to measure the ion signal in the absence of light. The light, propagating at a right angle to the cluster beam, is focused onto the beam axis by two lenses with focal lengths of 50 and 5 cm, respectively. For each wheel position (wavelength) the resulting energy-analyzed mass spectrum (see below) is routed into its proper part of computer memory. Typically, the total counts accumulated is the sum of about 100 full rotations of both wheels, each cycle lasting ~ 100 s. In this way it is assured that the measurements at different wavelengths are obtained under essentially identical conditions with respect to cluster-beam intensity and overlap of light and cluster beams.

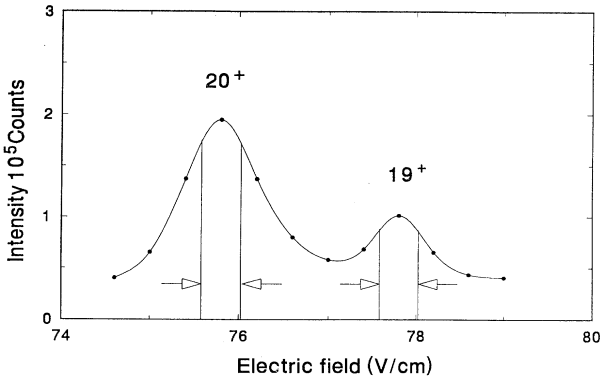

FIG. 1. Part of a mass spectrum obtained with the 0.25-T magnetic field by varying the electric field. The 2-mm defining slit is placed 1 m downstream from the velocity filter. The area between the arrows indicates the portion of the selected cluster beam that is used.

Photon absorption by a cluster leads to rapid evaporation[11] of one or more atoms. As a result, the kinetic energy of the daughter clusters is reduced to values of $2(1-x/N)$ keV, where x is the number of evaporated atoms and N is the number of atoms in the parent cluster. The average velocity of the daughter clusters is not changed in the evaporation process, and recoil contributions, leading to a broadening of the velocity distribution, can be neglected. Thus, the daughter clusters can be identified by measuring their respective kinetic energies, which are proportional to their masses. This is done by letting the clusters enter a 90° cylindrical electrostatic field 15 cm downstream from the irradiation zone. The clusters traverse the field region with different bending radii depending on their respective energies.

A fraction of the mass-selected clusters (about 5–20%) has preserved sufficient internal energy since their formation, or may acquire it from the ionization process or from collisions with rest-gas molecules, to evaporate atoms in flight between acceleration and irradiation. In order to reduce this background of lower-mass clusters a potential barrier, consisting of 16 electrodes, is placed after the 2-mm slit. It is adjusted to reject clusters that have lost about 20 eV (i.e., 1%) or more kinetic energy. Clusters that are able to overcome the potential barrier are again accelerated to 2 keV and focused by an Einzel lens built into the accelerating part of the barrier. On their way from the barrier to the ion detector (see below) clusters may, of course, still collide with rest-gas molecules. One finds that the relative amount of two or more atom evaporations is decreased by a factor of 3 by the barrier, corresponding to the reduction in flight path. For the one-atom evaporation the reduction is even

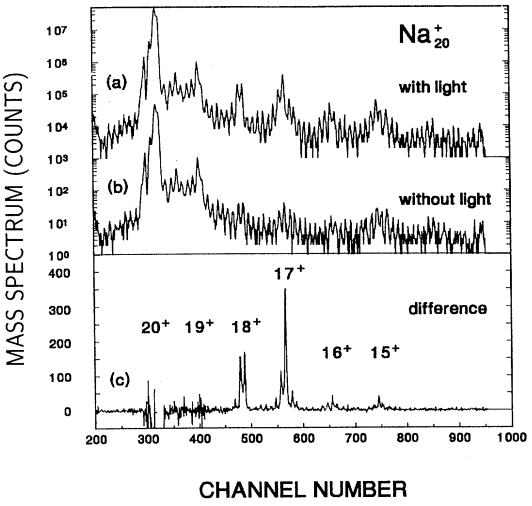

FIG. 2. (a) The mass spectrum measured with the MCP ion detector following irradiation of a Na_{20}^+ cluster beam with light through a BG38 filter (380–620 nm). The scale is shifted by 10^3. (b) The same as (a) without light irradiation. The daughter products are due to delayed evaporation and collisions with rest-gas moleculars. (c) The difference spectrum (a)−(b). By integrating the counts in the parent cluster, a depletion of $1.33\pm0.23\,\%$ is measured. A summing of the intensity of the daughter clusters, on the other hand, yields $1.25\pm0.02\,\%$, a vastly improved statistical accuracy. The loss of up to five atoms is due to the competition between monomer and dimer evaporation in the decay chain.

larger and amounts to about a factor of 10 with a characteristic odd-even staggering. We therefore ascribe this process to collisionless evaporation due to residual internal energy.

After leaving the field region, the cluster ions are detected by a position-sensitive microchannel plate (MCP) detector. It has an active diameter of 40 mm, but is collimated by a 40×10 mm^2 mask in front. The anode of the MCP consists of a printed circuit board with 80 strips (0.25×10 mm^2) at 0.5-mm intervals. Each anode strip is connected to its two neighbors via 2-ns delay lines. The two outer anode strips are fed into two fast amplifiers, followed by two constant fraction discriminators. By recording the time difference between the signals at both ends of the delay line, information about the detection position and, consequently, the kinetic energy of the incident cluster ion is obtained. The spatial resolution of the device is 0.5 mm. An example of an evaporation spectrum for Na_{20}^+ is shown in Fig. 2(a).

III. MEASUREMENTS AND DATA ANALYSIS

Following photon absorption, there is a depletion of the parent cluster beam due to evaporation of one or more atoms. Under the present experimental conditions, typical beam depletions for individual light filters are fractions of a percent. The statistical accuracy in a direct measurement of this depletion is bound to be poor. This is why we determine the cross section by detection of the evaporation products (daughter clusters).

For each wavelength, the number of daughter clusters is determined by integrating and summing the peaks corresponding to different evaporation products, after subtracting a background spectrum obtained without irradiation of the cluster beam (see Sec. II). Figure 2 illustrates this.

Absolute cross sections σ are obtained by taking into account the absolute intensities of both the cluster beam and the incident photon beam as well as their overlap. In our case of a wide photon beam and a narrow cluster beam,

$$\sigma(\lambda)=\frac{I_{\rm evap}(\lambda)}{I_0}\frac{1}{\Phi(\lambda)\tau}\ . \tag{1}$$

$I_{\rm evap}$ is the number of daughter clusters (s^{-1}), I_0 is the incident cluster-beam intensity (s^{-1}), τ is the overlap time between the cluster and the light beam (s), and Φ is the photon flux ($cm^{-2}s^{-1}$).

The number of daughter clusters $I_{\rm evap}$ is obtained from integrating the evaporation peaks in the difference spectrum, described above. I_0 is the number of parent clusters in the mass spectrum measured in the absence of light [Fig. 2(b)]. The overlap time can be written as $\tau=l/v$, where l is the overlap length and v is the cluster velocity; thus

$$\sigma=\frac{I_{\rm evap}}{I_0}\left[\frac{1}{\Phi l}\right]v\ . \tag{2}$$

The quantity Φl in the square brackets is determined by the flux of light transmitted through the interference filters and the fraction of transmitted photons overlapping with the cluster beam. The total number of photons transmitted through each of the filters are measured with a watt meter and are estimated to be in error by at most $\pm5\%$.

The differential overlap $\Phi(y)l(y)$ between the cluster beam and the light beam is determined in the following way. A beam of Na_{20}^+ clusters is irradiated with light in the broad wavelength interval, 380–620 nm (BG38 and IR-reflection filter), an interval covering the energy region where the plasmon is strongly excited. The 2-mm slit (see Sec. II) is moved vertically in steps of 1 mm. The transmission of the Na_{20}^+ cluster beam through the slit is maximized at each position of the slit by small adjustments of the voltage in the velocity filter. The measured relative photon absorption as a function of the slit position yields the overlap between the cluster beam and the light (see Fig. 3). The curve is assumed representative for all interference filters, neglecting the small change in focal length with λ. The total area represents the photon flux as measured by the watt meter for each filter. Thereafter the measured curve is corrected for the finite slit width of 2 mm by an unfolding procedure. In this way the absolution cross section in the broad wavelength interval is determined. Subsequently it is measured for each of the 15 narrow wavelength intervals.

For clusters other than Na_{20}^+ absolute cross sections

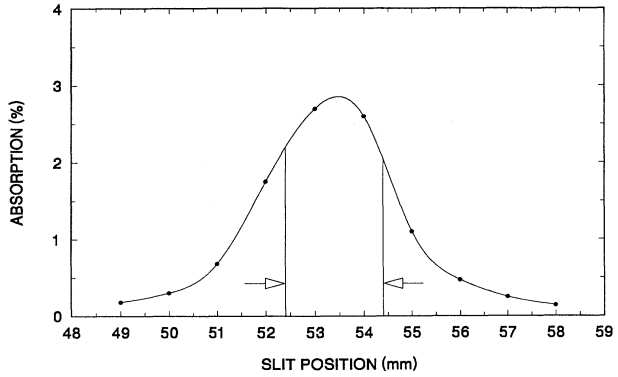

FIG. 3. The effective overlap of cluster and photon beam, obtained by sweeping the cluster beam (Na_{20}^+) across the stationary light beam. $2.00 < E_{h\nu} < 3.26$ eV. The slit size is indicated. The area between the arrows corresponds to 55% of the light as estimated through the unfolding procedure (see text).

are obtained through a measurement of relative yields. These are then normalized by using the absolute, broadband value for Na_{20}^+ in the following manner. Each mass-selected cluster size is irradiated with the xenon lamp through the same broadband filters described above, which covers more than 90% of the energy range of the plasmon excitation. The uncertainty of this fraction is due to different shapes of the plasmon resonance curves. It amounts to less than $\pm 5\%$ and is ignored in the following. The relative, broadband absorption cross sections are obtained from the number of daughter clusters formed after irradiation through these filters.

The results are shown in Fig. 4 as a function of cluster size N. The values increase with $(N-1)$, the number of valence electrons in the cluster, and with $\sqrt{N}$, which is proportional to the irradiation time of the cluster. The solid curve is proportional to $(N-1)\sqrt{N}$, and normalized to the experimental value for Na_{20}^+. From the data of Fig. 4, absolute cross sections σ can be obtained for all clusters.

Since ~ 2.6 eV is absorbed and the separation energies for atoms and dimers are 0.7–1.3 eV in the region[12]

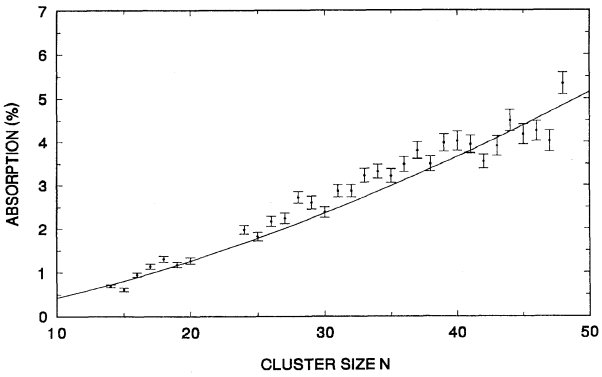

FIG. 4. Relative absorption yields measured with a broadband filter. The solid line is proportional to $\sqrt{N}(N-1)$, normalized at the experimental value for $N=20$.

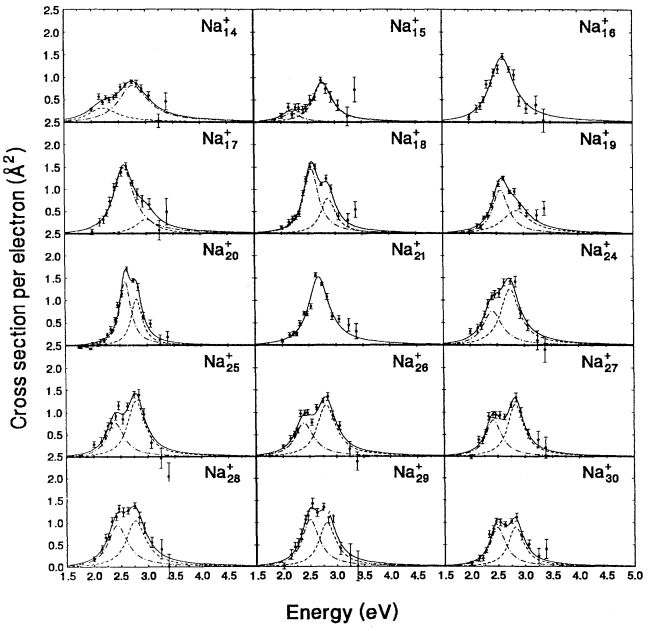

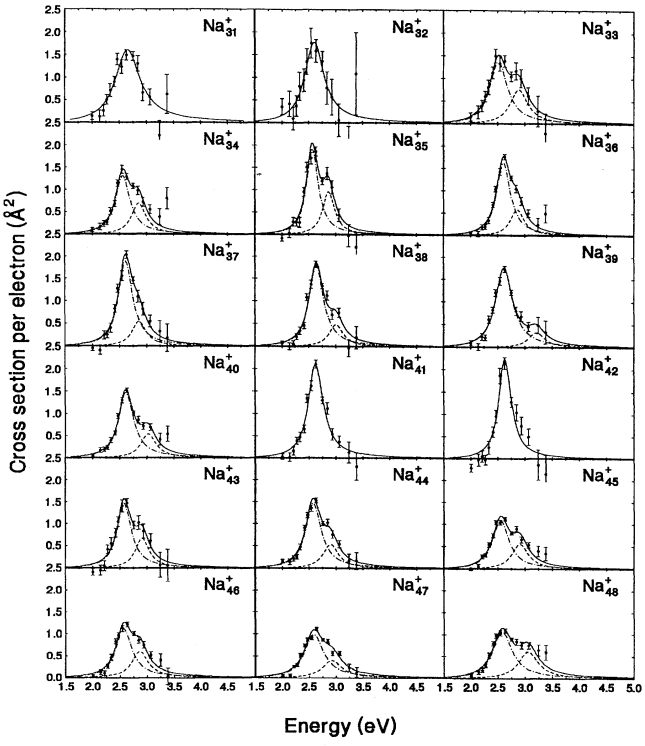

FIG. 5. Photoabsorption spectra normalized to the absolute cross section via Fig. 4. Note the generally larger uncertainties for the two points at the highest photon energies due to low filter transmissions. For negative cross-section values the full error bar is not always shown. No data were taken for $N=22$ and 23 because of insufficient cluster-beam intensity. The curves are Lorentz functions fitted to the data.

there is sufficient *energy* available to evaporate at least two atoms. The *time* available for evaporation ($\simeq 1.4\sqrt{N}$ μs) need not cover the complete decay chain; as long as just one atom is evaporated a daughter product will appear in the spectrum and be included in the cross section. In the majority of the cases we observe two- and three-atom evaporations; only for the heaviest clusters does single-atom evaporation begin to be of some importance ($\approx 15\%$ for $N=48$).

The photoabsorption spectra for all clusters studied ($N=14$ to 48) are shown in Fig. 5. Cross sections are depicted as a function of photon energy. The error bars on the data points include the statistical uncertainties only. In addition to this there is the possible systematic error of less than $\pm 5\%$ in the determination of the photon flux and an estimated $\pm 5\%$ uncertainty in the normalization procedure.

IV. RESULTS

Oscillator strengths

The collectivity of the resonance peaks in Fig. 5 can be gauged through their contribution to the dipole sum rule. The total cross section per valence electron for dipole transitions (the sum rule) is given by[13]

$$\int \sigma(E)dE = \frac{2\pi^2 e^2 \hbar}{mc} = 1.0975 \text{ eV Å}^2/\text{electron} . \quad (3)$$

For a given cluster, the total cross section is determined by integrating the resonance curve over the 15 measured data points:

$$\sigma_{\text{tot}} \simeq \sum_{i=1}^{15} \sigma(E_i)\Delta E_i . \quad (4)$$

$\sigma(E_i)$ is the cross section of the ith data point at energy E_i, ΔE_i is the energy interval from $(E_i+E_{i-1})/2$ to $(E_i+E_{i+1})/2$ centered approximately at the mean energy E_i. The resulting values of σ_{tot} are shown in Fig. 6, expressed relative to the total strength of 1.0975 eV Å^2 per electron. On a 1σ confidence level, the error bars reflect the statistical uncertainties plus $\pm 5\%$ uncertainty in the normalization. The error bars do not include any systematic error that may be present in the determination of the absolute photon flux.

On the assumption that evaporation of atoms is the only decay channel, the experimentally determined cross sections are seen to exhaust between 70% and 100% of the dipole sum rule (with Na_{15}^+ as the exception). We conclude that the measured resonance curves indeed represent a collective electronic excitation, the surface plasmon.

Centroid energies

We extract the centroid energies $\langle E \rangle$ of the plasmon absorption spectra according to

$$\langle E \rangle = \frac{\sum_{i=1}^{15} E_i \sigma(E_i)\Delta E_i}{\sum_{i=1}^{15} \sigma(E_i)\Delta E_i} \quad (5)$$

with the quantities ΔE_i, E_i, and $\sigma(E_i)$ defined above. The centroid energies as a function of the cluster size are shown in Fig. 7. They turn out to be rather constant, with a mean value of 2.64 eV, over the size range considered.

This can be compared with the classical Mie-resonance energy

$$E_{\text{Mie}} = \hbar \left[\frac{e^2}{m r_s^3} \right]^{1/2} = 3.34 \text{ eV} . \quad (6)$$

where the Wigner-Seitz radius is taken to be $r_s = 2.16$ Å at 500 K.[14] Measurements of the bulk volume plasmon yields by division by $\sqrt{3}$ a somewhat lower value, 3.13 eV,[15] while the value obtained by multiplying the measured bulk planar surface plasmon energy of 3.99 eV by $\sqrt{2}/\sqrt{3}$ is 3.08 eV when corrected for temperature.[16] In other words the experimental bulk resonance energy is about 7% lower than the theoretical value, referred to the same temperature.

Our measured value of 2.64 eV is significantly redshifted compared to these values and this is currently under-

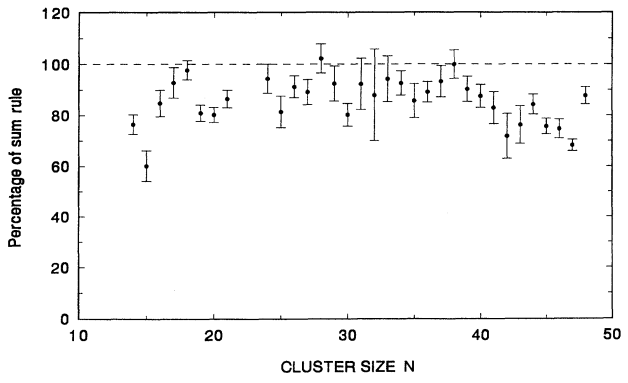

FIG. 6. Fraction of the dipole sum rule observed.

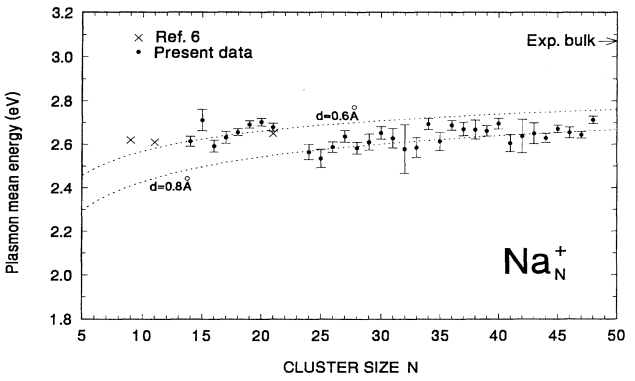

FIG. 7. Mean energy of the resonances of Fig. 5. The two curves are the expected variations for a constant $d=0.6$ and 0.8 Å, respectively. The bulk value indicated is extracted from a measurement of the (planar) surface plasmon (Ref. 16). × are experimental mean values by Bréchignac *et al.* (Ref. 6).

stood as an effect of the spill-out of the valence electrons.[4] On the other hand, if the electron distribution has a constant spill-out contribution d independent of cluster size, our measured value of $\langle E \rangle$ should increase with cluster size. The expected variation for two different values of d is indicated in Fig. 7. The curves converge towards the experimental bulk value for $N \rightarrow \infty$. As one sees, the experimental results indicate a tendency for the spill-out to increase from 0.6 to 0.8 Å as the size increases from $N = 14$ to 48. Perhaps it is not unreasonable to imagine that the positive charge on the cluster ions could have that effect on the spill-out. If so, the resonance energies measured for neutral sodium clusters should be slightly redshifted compared to ours. Photoabsorption on Na_{20} shows a mean resonance energy of 0.15 eV lower than the present value for Na_{21}^+.[8] Also a qualitative comparison with more extended data set of Ref. 2 indeed shows the anticipated redshift. For further discussion of the redshifts, see Ref. 3. The present results differ markedly from measurements on neutral sodium clusters (size 10 to

TABLE I. Values derived from the Lorentz functions. Fitting parameters from Eq. (8) (Cols. 2–6). The area ratio is height1/height2 (col. 7). The axis ratio $R_\perp/R_z$ is derived through Eqs. (9) and (10) (col. 8).

Cluster size, N	Energy1 (eV)	Energy2 (eV)	Width (eV)	Height1	Height2	Area ratio	Axis ratio
14	2.21(4)	2.77(2)	0.65(7)	0.32(5)	0.83(4)	0.39(6)	0.73(2)
15	2.20(8)	2.77(2)	0.42(6)	0.21(5)	0.87(5)	0.24(6)	0.73(3)
16	2.62(1)		0.54(3)	1.44(5)			1
17	2.58(1)	2.99(10)	0.45(4)	1.48(8)	0.33(13)	4.48(178)	1.35(12)
18	2.55(1)	2.87(1)	0.33(2)	1.46(4)	0.80(8)	1.83(19)	1.26(2)
19	2.58(1)	2.88(3)	0.38(3)	1.13(5)	0.46(9)	2.46(49)	1.23(3)
20	2.60(1)	2.81(1)	0.25(1)	1.43(7)	1.03(9)	1.39(14)	1.15(1)
21	2.68(1)		0.46(2)	1.52(4)			1
24	2.41(2)	2.74(2)	0.42(2)	0.75(6)	1.25(9)	0.60(6)	0.83(1)
25	2.40(2)	2.78(2)	0.39(4)	0.77(8)	1.26(8)	0.61(7)	0.81(1)
26	2.39(1)	2.81(1)	0.42(1)	0.76(4)	1.16(5)	0.66(4)	0.79(1)
27	2.42(1)	2.83(1)	0.36(1)	0.82(3)	1.18(5)	0.69(4)	0.80(1)
28	2.43(1)	2.77(2)	0.44(3)	0.95(9)	1.05(5)	0.90(10)	0.82(1)/1.29(3)
29	2.50(2)	2.81(3)	0.39(2)	1.07(11)	0.99(9)	1.08(14)	0.84(2)/1.25(4)
30	2.48(1)	2.82(2)	0.35(3)	0.89(7)	0.90(8)	0.99(12)	0.83(1)/1.29(2)
31	2.65(1)		0.56(3)	1.68(8)			1
32	2.60(2)		0.43(7)	1.78(20)			1
33	2.51(2)	2.89(4)	0.39(5)	1.38(13)	0.76(19)	1.82(49)	1.33(5)
34	2.56(1)	2.85(3)	0.32(3)	1.31(8)	0.69(11)	1.90(32)	1.23(3)
35	2.56(1)	2.87(2)	0.27(2)	1.91(11)	0.96(13)	1.99(29)	1.25(2)
36	2.60(1)	2.86(2)	0.31(1)	1.63(4)	0.58(5)	2.81(25)	1.20(2)
37	2.60(2)	2.85(7)	0.32(3)	1.89(14)	0.54(22)	3.50(145)	1.19(6)
38	2.63(1)	3.00(4)	0.32(2)	1.79(7)	0.47(10)	3.81(81)	1.30(4)
39	2.61(1)	3.21(10)	0.38(2)	1.75(6)	0.32(13)	5.40(220)	1.60(17)
40	2.61(1)	3.02(2)	0.34(1)	1.75(5)	0.64(6)	2.73(30)	1.34(3)
41	2.62(1)		0.34(2)	2.09(8)			1
42	2.63(1)		0.28(2)	2.23(12)			1
43	2.57(1)	2.90(4)	0.31(3)	1.46(11)	0.66(15)	2.21(53)	1.26(4)
44	2.57(1)	2.90(3)	0.35(2)	1.47(6)	0.53(9)	2.77(48)	1.26(3)
45	2.55(1)	2.90(2)	0.37(2)	1.08(4)	0.55(6)	1.96(23)	1.29(2)
46	2.56(1)	2.86(2)	0.36(2)	1.11(6)	0.60(4)	1.85(16)	1.24(2)
47	2.58(2)	2.92(6)	0.40(8)	0.99(6)	0.40(8)	2.48(52)	1.27(7)
48	2.57(1)	3.05(8)	0.44(3)	1.06(5)	0.61(7)	1.74(22)	1.44(11)

300) adsorbed on a surface because they show an increase of no less than ≈ 0.4 eV in the plasmon energy in the interval from 14 to 48 atoms.[17]

Double-peak structures

As discussed in the Introduction, clusters with nonspherical shapes should absorb light at two or three different frequencies reflecting plasmon excitation along the different principal axes of the cluster. Measurements of the absorption profiles are therefore of special interest as a means of determining the cluster shapes.[1,5] Figure 5 shows that for a majority of the clusters the resonance is asymmetrically broadened, reflecting the existence of at least two components; furthermore, closer scrutiny of the data reveals a systematic alternation in the asymmetry. On the other hand, for the Na_{21}^+ and Na_{41}^+ clusters, which correspond to 20 and 40 valence electrons, respectively, the strength seems to be concentrated in a single peak. Thus, the data suggest an analysis in terms of the deformation picture.

The polarizability of a metal ellipsoid has different values along the three principal axes. For meal droplets much smaller that the wavelength of the incident photons and randomly oriented with respect to the photon polarization, the photon absorption spectrum can be expressed[18] as a sum of three resonances,

$$\sigma(E)=\sum_{i=1}^{3}\sigma_{0i}\frac{(E\Gamma_i)^2}{(E^2-E_{0i}^2)^2+(E\Gamma_i)^2}\ , \tag{7}$$

where σ_{0i}, Γ_i, and E_{0i} are the maximum amplitude, width, and energy, respectively, of each individual resonance.

We have performed an analysis of the photoabsorption spectra by fitting Lorentz functions to the shapes of the resonance. However, neither the number of data points nor their statistical accuracy justifies a fit based upon three independent Lorentz components. One or two Lorentz curves are sufficient to exhaust the information content of the data. In addition, a common width is chosen in cases of two Lorentz curves, in order to limit the number of free parameters. (Allowing for two independent widths does not increase the information gained from the fits, nor is there an improvement of the fit convergence in terms of reduced χ^2. It should be emphasized, however, that there is no obvious physical reason for choosing equal widths.)

The fitting function has the form

$$f(E)=\sum_{i=1}^{j}\frac{H_i W_i^2 E^2}{(E^2-E_i^2)^2+W_i^2E^2}\ , \tag{8}$$

where H_i, W_i, and E_i are the height, width, and resonance energy of each component, respectively. For single peaks $j=1$ and for double peaks $j=2$ with $W_1=W_2$.

The results of the fits are shown in Fig. 5 and the parameter values are listed in Table I. The peak resonance energies are determined to within $\pm 2\%$ (and are not affected beyond the uncertainties when six free parameters are used). The uncertainties in the widths are seen to be considerably larger (10–20 %).

It should be emphasized that the number of Lorentz components—one or two—is decided before making the computer fit; in most cases there is little or no ambiguity in this, but in some the choice is open to discussion. Also, the scatter of the two points at the highest photon energies does in some cases lead the fitting routine astray, resulting in parameters seemingly beyond the general systematics, e.g., Na_{39}^+.

V. DISCUSSION

The fitted resonance energies (Table I) are shown as a function of the cluster size in Fig. 8. A prolate shape is inferred when the intensity of the high-energy peak is approximately twice the intensity of the low-energy peak, and vice versa for oblate shapes. As a major result one finds that prolate and oblate shapes occur systematically in groups. For cluster sizes below Na_{17}^+ and between Na_{24}^+ and Na_{27}^+, the data indicate prolate shapes, while oblate shapes are indicated for Na_{17}^+ to Na_{20}^+, Na_{33}^+ to Na_{40}^+, and above Na_{42}^+.

As a more quantitative test of this interpretation the ratios of the areas under the two Lorentz curves, A_1/A_2, are shown in Fig. 9. In the simplest picture of a spheroidally deformed metal drop, the ratio should be $\frac{1}{2}$ and 2 for prolate and oblate shapes, respectively. Considering the experimental uncertainties the data are consistent with the assumed axially symmetric distortions.

Single-peaked resonances occur around the magic electron numbers 20 and 40, and possibly at the transition between prolate and oblate shapes at Na_{16}^+ and at Na_{31}^+ and Na_{32}^+.

The Na_{21}^+ resonance has been studied in two other experiments, one of which shows a very narrow double-peak structure,[6] whereas the other does not.[19] While the present data agree very well with those of Ref. 19, our resolution is not sufficient to reveal the double structure reported in Ref. 6.

The Na_{41}^+ resonance was also studied in Ref. 19 and fitted by the authors with two (unresolved) Lorentz curves and a high-energy shoulder. Their peak cross section is lower than the present by $\sim 25\%$ but has a mean

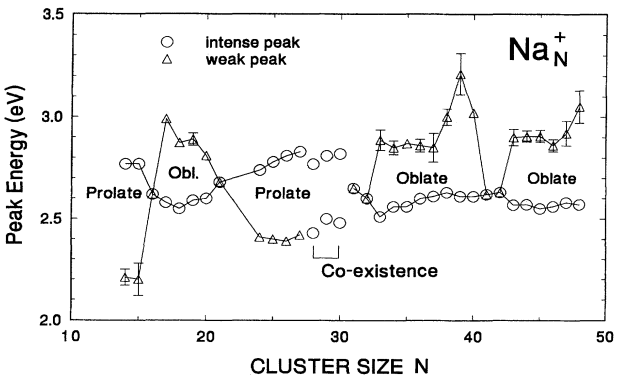

FIG. 8. Fitted peak resonance energies as a function of cluster size. The intense (doubly degenerate) peaks are shown as circles, the weaker ones as triangles. Only error bars larger than the symbols are shown.

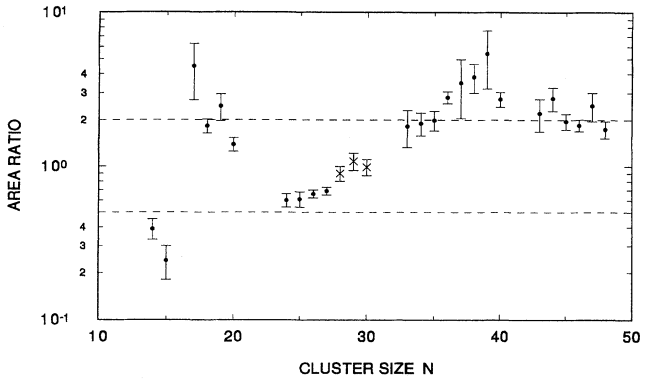

FIG. 9. The ratio of the areas under the two Lorentzian components A_1/A_2, as a function of cluster size, where A_1 and A_2 are the areas under the lower- and higher-energy components, respectively. The values for $28 \leq N \leq 30$ are shown by crosses (see text).

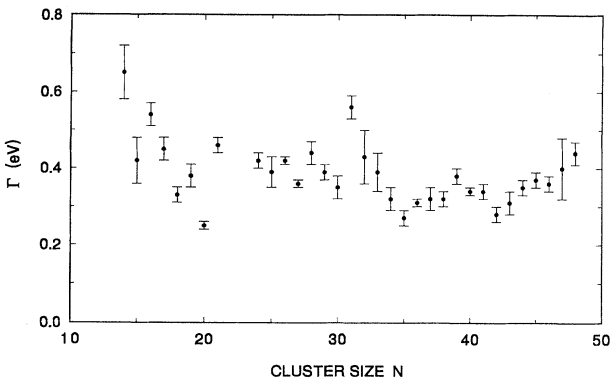

FIG. 11. The widths of the fitted functions as a function of cluster size.

energy of the same value (2.6 eV). There is considerable strength on the high-energy side of the peak in Ref. 19, not observed in our case; the authors trace the differences to a temperature effect. Yannouleas[9] points out that in his model calculations for a Na_{41}^+ cluster the resonance splits into two peaks at 2.9 and 3.3 eV with intensities 54% and 31%, respectively; this is not observed.

The single-peaked resonances at cluster sizes $N=16$ and 31 to 32 may also be due to sphericity, although they are not connected to the magic electron numbers 20 and 40 (Fig. 10). Another explanation may be triaxility, which is to be anticipated in the transition between regions of oblate and prolate shapes. Since the widths of these resonances are larger than average (Fig. 11) one may interpret them as three equally intense but closely lying peaks, a response one would expect from a triaxial cluster. Experiments with higher resolution and better statistics are needed to resolve this question.

The three clusters Na_{28}^+, Na_{29}^+, and Na_{30}^+ show two peaks with essentially equal areas (heights), Fig. 5. These clusters also lie in the transition region from prolate to oblate shapes. One may therefore hypothesize that these

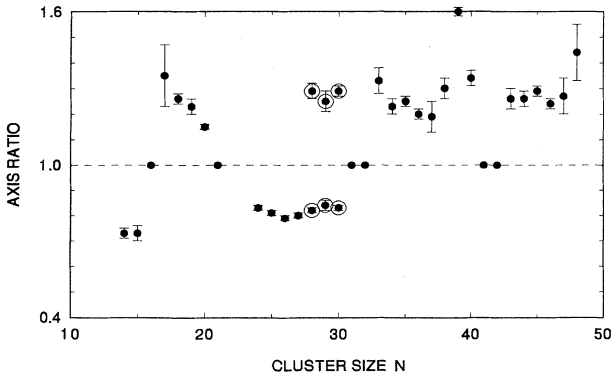

FIG. 10. Ratios of axes, $R_\perp/R_z$, perpendicular and parallel with the cluster symmetry axis. For $N=28$, 29, and 30 the points have less meaning as the weaker peak in the resonances is hidden.

clusters are indeed deformed, but the prolate equilibrium shape lies close in energy (within $k_B T$) to the oblate energy minimum, T being the temperature of the cluster. With equal population of two such isomers a spectrum with two equally high peaks will actually result, as observed. It is interesting that theoretical calculations of the equilibrium deformations give qualitative support to this interpretation.[20]

Assuming a spheroidal jellium model, Lipparini and Stringari[21] have derived an approximate expression for the relation between the ratios of the two resonance energies $E_\perp$ and E_z and the two axis lengths $R_\perp$ and R_z, respectively, where z indicates the symmetry axis

$$\frac{E_z}{E_\perp} \simeq 1-\tfrac{3}{5}\delta \tag{9}$$

with the deformation defined as

$$\delta \equiv \frac{3}{2}\left[\frac{R_z^2-R_\perp^2}{R_z^2+2R_\perp^2}\right] . \tag{10}$$

The last column in Table I lists the axis ratios calculated from the two resonance energies using the above formulas, and in Fig. 10 the values are plotted. For cluster sizes 28 to 30 two values are shown, reflecting our interpretation in terms of coexistence of oblate and prolate shapes.

Values of the experimental distortion parameter, $2(1-R_\perp/R_z)/(1+R_\perp/R_z)$, are displayed in Table II and compared to various model calculations: a modified Nilsson Hamiltonian,[5] an ellipsoidal shell model,[22] a self-consistent spheroidal jellium model,[23] self-consistent Kohn-Sham calculations including exchange and correlation energies in the local-density approximation for diffuse jellium[24] and Nilsson[25] models, and finally the Strutinsky method used with a Woods-Saxon potential with quadrupole, octupole, and hexadecapole deformations included.[20]

From Table II it is obvious that all models predict the region $N=17$ to 27 fairly well, especially if it is not the precise size of, more the trend in deformations, that is considered. The same accounts for the region $N=34$ to

41 albeit to a somewhat lesser extent. The disagreement between experiment and the models is most strongly exhibited in the prolate to oblate transitions, $N=14$ to 16 and $N=31$ to 33, and for the oblate deformations, $N \geq 43$.

The width of a plasmon resonance is in principle a sensitive measure of the mechanisms responsible for its damping. The widths of the Lorentz functions extracted from the fits are shown in Fig. 11. Two main mechanisms may contribute to the damping width. In a microscopic description the collective excitation consists ideally of a single coherent superposition of a number of single-electron transitions. In realistic calculations the collective strength is (Landau) fragmented among a number of more or less close-lying states, centered around the ideal resonance energy. According to such calculations this Landau fragmentation may be of the orders of 0.5–1.0 eV (Ref. 9) and therefore not negligible with the present experimental resolution. Landau fragmentation may be responsible for the additional strength on the high-energy side of the main resonance peak, especially for cluster sizes 43 through 48 (see Fig. 5). Landau fragmentation is essentially independent of temperature.[26–28]

The other part contributing to the width is the coupling to the thermal fluctuations of the ionic core and the associated shape fluctuations. This effect is proportional to $T^{1/2}$.[29] Therefore, experiments performed at several different cluster temperatures should be able to distinguish between the two types of peak broadening. Recent measurements on Na_{21}^+ and Na_{41}^+ at two different temperatures[19] are not incompatible with a $T^{1/2}$ dependence of the widths. Also, the plasmon resonance of hot K_{21}^+ clusters has been measured and compared to results from cold potassium clusters;[30] the authors conclude that the width can be largely explained by thermal fluctuations. Therefore the present observed widths of the peaks are on the whole believed to be caused by thermal fluctuations of the cluster shape.

As argued in Sec. IV (Fig. 6) the surface plasmon accounts for the major oscillator strength of dipole transitions involving the valence electrons. Kresin[31] has discussed the importance of the volume plasma excitations relative to the surface mode. For neutral clusters in the present mass range the volume plasmon mode is estimated to contribute $\sim 20\%$ of the total dipole excitation. Its energy is estimated to be ~ 4.3 eV and thus outside our experimental range.

TABLE II. The experimental distortion parameter (for Na_N^+) compared with theoretical models (for Na_{N-1}). The values in parentheses (col. 4) are actually triaxial deformations (Ref. 22) where we have taken a mean of the two axes closest in size.

N	Expt.	Ref. 5	Ref. 22	Ref. 23	Ref. 24	Ref. 25	Ref. 20
14	0.31	0.42	(−0.45)			−0.40	0.50
15	0.31	−0.49	−0.50	−0.56	−0.55	0.35	0.52
16	0	−0.41	(−0.42)			−0.25	0.41
17	−0.30	−0.33	(−0.34)		−0.36	−0.35	−0.38
18	−0.23	−0.27	(−0.29)			−0.30	−0.33
19	−0.21	−0.21	−0.24	−0.17	−0.24	−0.20	−0.27
20	−0.14	0	−0.11	0		0	0
21	0	0	0	0	0	0	0
24	0.19	0.26	(0.29)			0.25	0.21
25	0.21	0.30	(0.33)		0.32	0.30	0.23
26	0.23	0.33	(0.36)			0.35	0.29
27	0.22	0.36	0.39	0.37	0.40	0.35	0.33
31	0	0.30	(−0.36)		0.32	0.30	0.31
32	0	0.29	(−0.35)			0.30	0.31
33	0.28	−0.29	(−0.33)		−0.30	−0.30	0.30
34	−0.21	−0.26	(−0.32)			−0.30	−0.28
35	−0.22	−0.23	−0.31	−0.18	−0.26	−0.30	−0.28
36	−0.18	0.08	(−0.26)			−0.20	−0.22
37	−0.17	0.11	(−0.21)		.11	0.10	0.12
38	−0.26	−0.10	(−0.17)			−0.10	−0.13
39	−0.46	−0.10	−0.13	−0.09	−0.10	−0.10	−0.12
40	−0.29	−0.04	−0.06	−0.05		−0.05	
41	0	0	0	0	0	0	0
42	0	−0.04				−0.05	0.04
43	−0.23	−0.26				−0.25	0.11
44	−0.23	−0.11				−0.20	0.13
45	−0.25	−0.14				−0.15	0.16
46	−0.21	−0.15				0.20	0.19
47	−0.24	0.21				0.25	0.21
48	−0.36	0.22				0.25	0.23

VI. SUMMARY AND CONCLUSION

The measured photon absorption spectra of charged Na clusters, size 14 to 48, have been identified as the surface-plasmon resonance. The shape of the resonances and their systematic variation are interpreted in terms of deformations and as such the first observation, to our knowledge, of cluster shapes over nearly two major shells. They are on the whole found to be in quite good agreement with predictions based on theoretical mean-field models. The widths of the resonances are believed to be caused by thermal fluctuations, rather than Landau fragmentation. Additional measurements with very cold clusters could help distinguish between the two broadening mechanisms.

ACKNOWLEDGMENTS

We are obliged to Sven Bjørnholm for his lasting inspiration during this work, and we thank Hellmut Haberland for communicating the results of his group prior to publication. We also thank Stephanie M. Reimann and Thomas Hirschmann for letting us quote unpublished results of their calculations. This work was supported in part by U.S. DOE Contract No. DE-FG02-91ER-40609, the Danish Natural Science Research Council, the Carlsberg Foundation, and the NOVO Foundation.

*On leave from Yale University, New Haven, CT 06511.
†Present address: Ecole des Mines, F-54000 Nancy, France.
‡Present address: Danish Institute of Fundamental Metrology, 2800 Lyngby, Denmark.
§On leave from Institut für Kernchemie, Universität Mainz, D-6500 Mainz, Germany.

[1]W. D. Knight, K. Clemenger, W. A. de Heer, W. A. Saunders, M. Y. Chou, and M. L. Cohen, Phys. Rev. Lett. **52**, 2141 (1984).
[2]K. Selby, V. Kresin, J. Masui, M. Vollmer, W. A. de Heer, A. Scheidemann, and W. Knight, Phys. Rev. B **43**, 4565 (1991).
[3]W. A. de Heer, Rev. Mod. Phys. **65**, 611 (1993).
[4]M. Brack, Rev. Mod. Phys. **65**, 677 (1993).
[5]K. Clemenger, Phys. Rev. B **32**, 1359 (1985); Ph.D. thesis, University of California, Berkeley, 1958.
[6]C. Bréchignac, Ph. Cahuzac, F. Carlier, M. de Frutos, and J. Leygnier, Chem. Phys. Lett. **189**, 28 (1992).
[7]J. Tiggesbaümker, L. Köller, H. O. Lutz, and K. H. Meiwes-Broer, Chem. Phys. Lett. **190**, 42 (1992).
[8]S. Pollack, C. R. C. Wang, and M. M. Kappes, J. Chem. Phys. **94**, 2496 (1991).
[9]C. Yannouleas, Chem. Phys. Lett. **193**, 587 (1992).
[10]J. Pedersen, J. Borggreen, P. Chowdhury, N. Kebaïli, L. Lundsberg-Nielsen, K. Lützenkirchen, M. B. Nielsen, and H. D. Rasmussen, Z. Phys. D **26**, 281 (1993).
[11]C. E. Klots, J. Chem. Phys. **83**, 854 (1985).
[12]C. Bréchignac, Ph. Cahuzac, J. Leygnier, and J. Weiner, J. Chem. Phys. **90**, 1492 (1989).
[13]C. Yannouleas and R. A. Broglia, Phys. Rev. A **44**, 5793 (1991).
[14]*Handbook of Chemistry and Physics,* 60th ed. (CRC, Boca Raton, FL, 1981).
[15]A. vom Felde, J. Sprösser-Prou, and J. Fink, Phys. Rev. B **40**, 10 181 (1989).
[16]K. D. Tsuei, E. W. Plummer, and P. J. Feibelman, Phys. Rev. Lett. **63**, 2256 (1989).
[17]J. H. Parks and S. A. McDonald, Phys. Rev. Lett. **62**, 2301 (1989).
[18]A. Bohr and B. R. Mottelson, *Nuclear Structure* (Benjamin, Reading, 1975), Vol. II, p. 477.
[19]Th. Reiners, Ph.D. thesis, University of Freiburg, 1992; C. Ellert, H. Haberland, W. Orlik, Th. Reiners, and M. Schmidt (unpublished).
[20]S. Frauendorf and V. V. Pashkevich, Z. Phys. D (to be published).
[21]E. Lipparini and S. Stringari, Z. Phys. D **18**, 193 (1991).
[22]K. Selby, M. Vollmer, J. Masui, V. Kresin, W. A. de Heer, and W. D. Knight, Phys. Rev. B **40**, 5417 (1989).
[23]W. Ekardt and Z. Penzar, Phys. Rev. B **38**, 4273 (1988).
[24]Th. Hirschman, J. Meyer, and M. Brack (unpublished); Th. Hirschman, Ph.D. thesis, University of Regensburg, Germany, 1991.
[25]S. M. Reimann, Ph.D. thesis, University of Regensburg, Germany, 1992 and (private communication).
[26]Theoretical predictions (Refs. 27 and 28) give a smooth $1/R$ dependence of the Landau width for large ($N > 100$), spherical clusters. A $1/R$ fit to our data yields a value of the width which, when extrapolated to large R values, closely corresponds to the theoretical estimate for Landau damping alone. This coincidence is suggestive but may be purely accidental since the model is not expected to apply to the small and charged clusters studied here.
[27]G. Yannouleas and R. Broglia, Ann. Phys. **217**, 105 (1992).
[28]A. Kawabata and R. Kubo, J. Phys. Soc. Jpn. **21**, 1765 (1966).
[29]G. F. Bertsch and D. Tomańek, Phys. Rev. B **40**, 2749 (1989).
[30]N. Dam and W. A. Saunders, Z. Phys. D **19**, 85 (1991).
[31]V. Kresin, Phys. Rep. **220**, 1 (1992).